

# On Scale Space Radon Transform, Properties and Image Reconstruction

Nafaa Nacereddine<sup>a,\*</sup>, Djemel Ziou<sup>b</sup>, Aicha Baya Goumeidane<sup>a</sup>

<sup>a</sup>Research Center in Industrial Technologies CRTI, P.O.Box 64, Chéraga, Algiers 16014, Algeria

<sup>b</sup>DMI, Université de Sherbrooke, Québec, QC J1K 2R1, Canada

---

## Abstract

Aware of the importance of the good behavior in the scale space that a mathematical transform must have, we depict, in this paper, the basic properties and the inverse transform of the Scale Space Radon Transform (SSRT). To reconstruct the image from SSRT sinogram, the Filtered backprojection (FBP) technique is used in two different ways: (1) Deconvolve SSRT to obtain the estimated Radon transform (RT) and then, reconstruct image using classical FBP or (2) Adapt FBP technique to SSRT so that the Radon projections spectrum used in classical FBP is replaced by SSRT and Wiener filtering, expressed in the frequency domain. Comparison of image reconstruction techniques using SSRT and RT are performed on Shepp-Logan head phantom image. Using the Mean Absolute Error (MAE) as image reconstruction quality measure, the preliminary results present an outstanding performance for SSRT-based image reconstruction techniques compared to the RT-based one. Furthermore, the method (2) outperforms the method (1) in terms of computation time and adaptability for high level of noise when fairly large Gaussian kernel is used.

**Keywords:** Scale space Radon transform, SSRT properties, SSRT inversion, Deconvolution, Filtered back projection, Image reconstruction

---

## 1. Introduction

Scale Space Radon Transform (SSRT), introduced recently in [1], is a matching of an embedded shape in an image and the Gaussian kernel. The choice of the latter should satisfy several requirements such as nice behaviour in scale space, robustness to noise, uniqueness of transform maximum, etc. [1]. It follows that Radon transform [2] is a particular case of SSRT where, the Gaussian kernel is replaced by a Dirac distribution  $\delta$ .

As for the Radon transform, several properties could be derived from SSRT and which could be very useful in computer vision applications such as remote sensing, in-

---

\*Corresponding author

Email addresses: n.nacereddine@crti.dz (Nafaa Nacereddine),  
djemel.ziou@usherbrooke.ca (Djemel Ziou), a.goumeidane@crti.dz (Aicha Baya Goumeidane)

dustrial tomography and medical imaging. In this paper, some basic properties of SSRT will be presented. Furthermore, the approaches of SSRT inversion will be discussed where, a new version of Filtered Backprojection (FBP) [3, 4] dedicated to SSRT will be developed in detail and compared on "Shepp-Logan" image reconstruction results.

The remainder of the paper is organized as follows. The definition of SSRT and its relationship with Radon transform are depicted in Section 2. Section 3 is devoted to the SSRT properties including its inversion. Image reconstruction using SSRT is detailed in Section 4 and main experiments and results are reported in Section 5. Lastly, main conclusions are drawn in Section 6.

## 2. Scale Space Radon Transform

### 2.1. Definition

Let  $(x, y)$  the Cartesian coordinates of a point in a 2-D space,  $f(x, y)$  a continuous function with a compact support and  $g_{\Delta, \theta}$  a set of parallel linear Gaussians  $g_{\theta}(r - \rho, \sigma)$ , parameterized by the orientation angle  $\theta$ , the standard deviation  $\sigma$  and the centerline ( $\Delta$ ):  $x \cos \theta + y \sin \theta - \rho = 0$ , as illustrated in Fig. 1. By referring to Fig. 1, Scale Space Radon transform (SSRT), noted  $\mathfrak{R}_{\sigma}(\rho, \theta)$ , is define by [1]

$$\mathfrak{R}_{\sigma}(\rho, \theta) = \int_{-\infty}^{+\infty} \int_{-\infty}^{+\infty} f(x, y) g(x \cos \theta + y \sin \theta - \rho) dx dy \quad (1)$$

where,  $g(t) = \frac{1}{\sqrt{2\pi}\sigma} e^{-\frac{t^2}{2\sigma^2}}$  is the Gaussian function.

### 2.2. Its relationship with Radon transform

Let consider a  $(r, s)$  coordinate system, as in Fig. 1, a rotated version of the original  $(x, y)$  system, expressed as

$$\begin{bmatrix} r \\ s \end{bmatrix} = \begin{bmatrix} \cos \theta & \sin \theta \\ -\sin \theta & \cos \theta \end{bmatrix} \begin{bmatrix} x \\ y \end{bmatrix} \quad (2)$$

It follows that the SSRT is rewritten as

$$\mathfrak{R}_{\sigma}(\rho, \theta) = \int_r \int_s f(r \cos \theta - s \sin \theta, r \sin \theta + s \cos \theta) g(r - \rho) dr ds \quad (3)$$

Equivalently,

$$\mathfrak{R}_{\sigma}(\rho, \theta) = \int_r g(r - \rho) \left[ \int_s f(r \cos \theta - s \sin \theta, r \sin \theta + s \cos \theta) ds \right] dr \quad (4)$$

Note that the expression between brackets is nothing but the expression of the Radon transform  $\mathcal{R}(\rho, \theta)$ . It follows that

$$\mathfrak{R}_{\sigma}(\rho, \theta) = \int_r g(r - \rho) \mathcal{R}(\rho, \theta) dr = (g *^{\rho} \mathcal{R})(\rho, \theta) \quad (5)$$

where  $*^{\rho}$  is the convolution operation with regards to (w.r.t.) the variable  $\rho$ .

The formulae (5) constitutes a straightforward way to compute the SSRT which is nothing but the convolution of Radon transform with a Gaussian kernel tuned by a scale parameter  $\sigma$ . Consequently, the SSRT implementation is reduced to a convolution operation.

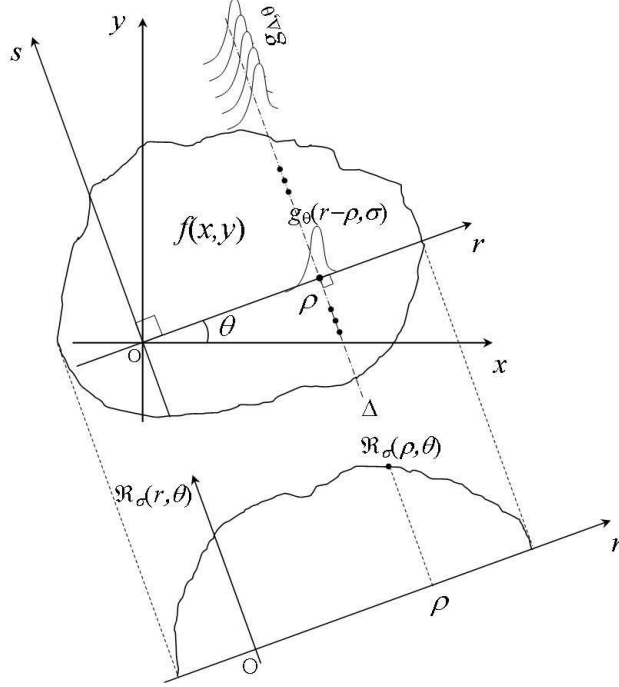


Figure 1: Definition of the Scale Space Radon Transform

### 3. SSRT Properties

#### 3.1. Basic Properties

In order to better handle the equations dealing with the SSRT properties, let us define the unitary vectors in the plan  $(r-s)$  axes, as  $\xi = [\cos \theta \ \sin \theta]^t$  and  $\xi^\perp = [-\sin \theta \ \cos \theta]^t$ , the position vector as  $z = [x \ y]^t$  and  $dz = dx dy$ . First, observe that the equation of the line  $(\Delta)$ , in Fig. 1, may be written  $\rho = \xi^t z = x \cos \theta + y \sin \theta$  and then the SSRT can be rewritten as

$$\mathfrak{R}_\sigma(\rho, \xi) = \int f(z) g_\sigma(\xi^t z - \rho) dz \quad (6)$$

Several elementary properties of the SSRT of a function  $f$  defined in  $\mathbb{R}^2$  follow directly from the definition.

##### 3.1.1. Linearity

Let us consider two functions  $f$  and  $g$  and two real numbers  $a$  and  $b$ . We have, then

$$\begin{aligned} \mathfrak{R}_\sigma[af(z) + bg(z)](\rho, \xi) &= \int [af(z) + bg(z)] g_\sigma(\xi^t z - \rho) dz \\ &= a \mathfrak{R}_\sigma[f(z)](\rho, \xi) + b \mathfrak{R}_\sigma[g(z)](\rho, \xi) \end{aligned} \quad (7)$$

### 3.1.2. Homogeneity

If  $a$  is a non-zero real number, then we have

$$\begin{aligned}\mathfrak{R}_\sigma(a\rho, a\xi) &= \int f(\mathbf{z}) g_\sigma(a\xi^t \mathbf{z} - a\rho) d\mathbf{z} = \frac{1}{|a|} \int f(\mathbf{z}) g_{\sigma/|a|}(\xi^t \mathbf{z} - \rho) d\mathbf{z} \\ &= \frac{1}{|a|} \mathfrak{R}_{\sigma/|a|}(\rho, \xi)\end{aligned}\quad (8)$$

Because of the presence of the amounts  $\sigma/|a|$  in the result, the property of homogeneity is not satisfied for the SSRT, except when  $|a| = 1$ , i.e.  $a = \pm 1$ . For  $a = 1$ , it consists in the identity transform whilst  $a = -1$  relates the case of symmetry in regards to the axes system origin. The last property will be detailed in the next paragraph.

### 3.1.3. Symmetry

Setting  $a = -1$  in (8) yields

$$\mathfrak{R}_\sigma(-\rho, -\xi) = \mathfrak{R}_\sigma(\rho, \xi) \quad (9)$$

In another notation, it means:  $\mathfrak{R}_\sigma(-\rho, \theta \pm \pi) = \mathfrak{R}_\sigma(\rho, \theta)$ .

### 3.1.4. Geometric transformation

Let  $\mathbf{z}$  and  $\mathbf{z}'$ , two vectors representing two points in  $\mathbb{R}^2$  space so that

$$\mathbf{z}' = \mathbf{A}\mathbf{z} \quad (10)$$

where  $\mathbf{A}$  is a nonsingular matrix with real elements representing the transfer matrix of geometric transformations such as scaling, rotation, shearing, etc.

$$\mathfrak{R}_\sigma[f(\mathbf{z}')](\rho, \xi) = \int f(\mathbf{A}\mathbf{z}) \cdot g_\sigma(\xi^t \mathbf{z} - \rho) d\mathbf{z} \quad (11)$$

Since  $\mathbf{z} = \mathbf{A}^{-1}\mathbf{z}'$  and  $d\mathbf{z} = |\mathbf{A}^{-1}| d\mathbf{z}'$  where  $|\cdot|$  denotes the matrix determinant, then, we obtain

$$\begin{aligned}\mathfrak{R}_\sigma[f(\mathbf{z}')](\rho, \xi) &= |\mathbf{A}^{-1}| \int f(\mathbf{z}') \cdot g_\sigma(\xi^t \mathbf{A}^{-1} \mathbf{z}' - \rho) d\mathbf{z}' = |\mathbf{A}^{-1}| \mathfrak{R}_\sigma(\rho, (\xi^t \mathbf{A}^{-1})^t) \\ &= |\mathbf{A}^{-1}| \mathfrak{R}_\sigma(\rho, \mathbf{A}^{-t} \xi)\end{aligned}\quad (12)$$

*Case of Rotation.* If  $\mathbf{A}$  is a matrix of rotation, i.e.  $\mathbf{A}^t = \mathbf{A}^{-1}$  and  $|\mathbf{A}^{-1}| = 1$ , we have

$$\mathfrak{R}_\sigma[f(\mathbf{z}')](\rho, \xi) = \mathfrak{R}_\sigma(\rho, \mathbf{A}^t \xi) \quad (13)$$

In other words, if  $\mathbf{A} = M_{Rot}^{\theta_0} = \begin{bmatrix} \cos \theta_0 & \sin \theta_0 \\ -\sin \theta_0 & \cos \theta_0 \end{bmatrix}$  then  $\mathbf{A}^t \xi = \begin{bmatrix} \cos(\theta + \theta_0) \\ \sin(\theta + \theta_0) \end{bmatrix}$ . In former notation, this means that

$$\mathfrak{R}_\sigma^{R_{\theta_0}}(\rho, \theta) = \mathfrak{R}_\sigma(\rho, \theta + \theta_0) \quad (14)$$

*Case of Scaling.* Let  $\mathbf{A} = \alpha \mathbb{I}$  where,  $\alpha$  ( $\alpha \in \mathbb{R}_+^*$ ) a scale factor, then  $\mathbf{A}^{-1} = \frac{1}{\alpha}$  and  $|\mathbf{A}^{-1}| = 1/\alpha^2$ . Hence, we obtain

$$\mathfrak{R}_\sigma[f(\mathbf{z}')](\rho, \boldsymbol{\xi}) = \frac{1}{\alpha^2} \mathfrak{R}_\sigma\left(\rho, \frac{\boldsymbol{\xi}}{\alpha}\right) \quad (15)$$

On the other hand,

$$\begin{aligned} \mathfrak{R}_\sigma[f(\mathbf{z}')](\rho, \boldsymbol{\xi}) &= \frac{1}{\alpha^2} \int f(\mathbf{z}') g_\sigma\left(\frac{\boldsymbol{\xi}'}{\alpha} \mathbf{z}' - \rho\right) d\mathbf{z}' = \frac{1}{\alpha^2} \int f(\mathbf{z}') g_\sigma\left[\frac{1}{\alpha}(\boldsymbol{\xi}' \mathbf{z}' - \alpha\rho)\right] d\mathbf{z}' \\ &= \frac{1}{\alpha^2} \int f(\mathbf{z}') [\alpha g_{\alpha\sigma}(\boldsymbol{\xi}' \mathbf{z}' - \alpha\rho)] d\mathbf{z}' = \frac{1}{\alpha} \mathfrak{R}_{\alpha\sigma}(\alpha\rho, \boldsymbol{\xi}) \end{aligned} \quad (16)$$

In terms of former notation, we have

$$\mathfrak{R}_\sigma^{S_\alpha}(\rho, \theta) = \frac{1}{\alpha} \mathfrak{R}_{\alpha\sigma}(\alpha\rho, \theta) \quad (17)$$

### 3.1.5. Translation

Let  $\mathbf{z}$ ,  $\mathbf{z}'$  and  $\mathbf{b}$  three vectors representing the coordinates of 3 points in  $\mathbb{R}^2$  space such as  $\mathbf{z}' = \mathbf{z} + \mathbf{b}$ . In order to find a relationship between the SSRTs of the functions  $f(\mathbf{z})$  and  $f(\mathbf{z}')$ , it suffices to write

$$\mathfrak{R}_\sigma[f(\mathbf{z}')](\rho, \boldsymbol{\xi}) = \int f(\mathbf{z} + \mathbf{b}) g_\sigma(\boldsymbol{\xi}' \mathbf{z} - \rho) d\mathbf{z} = \int f(\mathbf{z}') g_\sigma(\boldsymbol{\xi}' \mathbf{z}' - \boldsymbol{\xi}' \mathbf{b} - \rho) d\mathbf{z}' \quad (18)$$

which yields

$$\mathfrak{R}_\sigma[f(\mathbf{z}')](\rho, \boldsymbol{\xi}) = \mathfrak{R}_\sigma(\rho + \boldsymbol{\xi}' \mathbf{b}, \boldsymbol{\xi}) \quad (19)$$

Using another notation, if  $\mathbf{b} = [b_x \ b_y]'$  then the translation property can be expressed as

$$\mathfrak{R}_\sigma^{T_{\mathbf{b}}}(\rho, \theta) = \mathfrak{R}_\sigma(\rho + b_x \cos \theta + b_y \sin \theta, \theta) \quad (20)$$

### 3.2. Analytical Inversion

According to (5), we can write

$$\mathcal{R}(\rho, \theta) = \mathcal{F}_\rho^{-1} \left[ \frac{\mathcal{F}_\rho[\mathfrak{R}_\sigma(\rho, \theta)](\omega)}{\mathcal{F}_\rho[g(\rho)](\omega)} \right] (\rho, \theta) \quad (21)$$

where  $\mathcal{F}_\rho$  and  $\mathcal{F}_\rho^{-1}$  are, respectively, the 1D Fourier transform and its inverse with regards to the variable  $\rho$ . Let us recall that the inverse Radon transform theorem states that

$$f(x, y) = \frac{1}{2\pi^2} \int_0^\pi \int_{-\infty}^\infty \frac{\partial \mathcal{R}(\rho, \theta)}{\partial \rho} \frac{1}{x \cos \theta + y \sin \theta - \rho} d\rho d\theta \quad (22)$$

for  $0 \leq \theta < \pi$  and  $-\infty < \rho < \infty$ .

By substituting (21) in (22), we obtain

$$f(x, y) = \frac{1}{2\pi^2} \int_0^\pi \int_{-\infty}^\infty \frac{\partial \mathcal{F}_\rho^{-1} \left[ \frac{\mathcal{F}_\rho[\mathfrak{R}_\sigma(\rho, \theta)](\omega)}{\mathcal{F}_\rho[g(\rho)](\omega)} \right] (\rho, \theta) / \partial \rho}{x \cos \theta + y \sin \theta - \rho} d\rho d\theta \quad (23)$$

## 4. Image reconstruction using Scale Space Radon Transform

### 4.1. SSRT inversion through image deconvolution

The computation of the inverse Scale Space Radon Transform (iSSRT) through (23), evoked in Sect. III.b, is straightforward but is just given as an indication, since the deconvolution defined by the division in Fourier space is hazardous. On the basis of the link between the SSRT and the Radon transform, provided in (5), the inversion can be implemented in two steps:

- **Step 1:** Estimate the Radon transform  $\mathcal{R}()$  given the SSRT  $\mathcal{R}_\sigma()$  and the Gaussian function  $g()$  using an existing deconvolution algorithm.
- **Step 2:** Estimate the image function  $f()$  by using an existing RT inversion algorithm.

For Step 1, recent efficient deconvolution methods to estimate the Radon transform could be applied such as the Bayesian framework-based method proposed in [5]. About Step 2., dealing with image reconstruction from Radon projections, various approaches are investigated and developed by the researchers among them the popular Filtered Backprojection reconstruction method which is based on the Fourier Slice Theorem. With the aim to compare the reconstruction methods in terms of performance, the deconvolution scheme in [5], followed FBP, will be used later in the Experiments part.

In the next two subsections, we propose to go through the Fourier Slice Theorem (FST) and the Filtered Backprojection (FBP), commonly used with RT, in order to deal with the SSRT inversion.

### 4.2. Fourier Slice Theorem and Frequency-Domain Reconstruction used for SSRT

The 1-D Fourier transform of Radon transform w.r.t. to the variable  $\rho$ , noted  $P_\theta(\omega)$  is given by

$$P_\theta(\omega) = \mathcal{F}_\rho(\mathcal{R}(\rho, \theta)) = \int_{-\infty}^{+\infty} \mathcal{R}(\rho, \theta) e^{-i2\pi\omega\rho} d\rho \quad (24)$$

By substituting the Radon transform expression into (24), we obtain

$$P_\theta(\omega) = \int_{-\infty}^{+\infty} \left[ \int_{-\infty}^{+\infty} f(x, y) \delta(x \cos \theta + y \sin \theta - \rho) dx dy \right] e^{-2\pi\omega\rho} d\rho \quad (25)$$

where,  $\delta$  is the Dirac function.

Rearranging the order of integrals and using the sifting property of Dirac's delta function, gives

$$P_\theta(\omega) = \int \int_{-\infty}^{+\infty} f(x, y) e^{-i2\pi\omega(x \cos \theta + y \sin \theta)} dx dy \quad (26)$$

Comparing now this equation with the expression of the 2-D Fourier transform of  $f(x, y)$ :

$$\mathcal{F}(u, v) = \int \int_{-\infty}^{+\infty} f(x, y) e^{-i2\pi(ux + vy)} dx dy \quad (27)$$

We can remark that the right side of the expression  $P_\theta(\omega)$  represents the 2D Fourier transform of  $f(x,y)$  expressed in polar coordinates system of the Fourier plan, which results in the proposed statement

$$P_\theta(\omega) = \mathcal{F}(u,v)|_{u=\omega \cos \theta, v=\omega \sin \theta} = \mathcal{F}_{polar}(\omega, \theta) \quad (28)$$

Thus, in parallel-beam geometry, the Fourier Slice Theorem states that the 1-D Fourier transform  $P_\theta(\omega)$  of a projection  $\mathcal{R}(\rho, \theta)$ , obtained from the image  $f(x,y)$ , is identical to the central slice, at the angle  $\theta$ , of the 2-D image spectrum  $\mathcal{F}(u,v)$  [6].

Now, how could we apply the FST on the Scale Space Radon Transform? For this purpose, for given  $\theta$  and  $\sigma$ , let compute the 1-D Fourier of the SSRT w.r.t. the variable  $\rho$ . Using (5) and Fourier transform of the convolution we can write

$$P_{\theta,\sigma}(\omega) = \mathcal{F}_\rho[\mathcal{R}_\sigma(\rho, \theta)](\omega) = \mathcal{F}_\rho[g(\rho)](\omega) \cdot \mathcal{F}_\rho[\mathcal{R}(\rho, \theta)](\omega) = G(\omega)P_\theta(\omega) \quad (29)$$

where,  $G(\omega) = e^{-2\pi^2\sigma^2\omega^2}$  is the Fourier transform of the Gaussian function  $g$ .

Since, the FST deals with the Radon projections, the spectrum of the latter, which is linked to the 2-D Fourier transform of  $f(x,y)$  as seen above, can be then deduced from the SSRT projections as

$$P_\theta(\omega) = P_{\theta,\sigma}(\omega)/G(\omega) = P_{\theta,\sigma}(\omega)/e^{-2\pi^2\sigma^2\omega^2} \quad (30)$$

We can see, for small values of  $G(\omega)$  i.e., for very large values of  $\sigma$  and/or  $\omega$ , that computing  $P_\theta(\omega)$  by (30) becomes problematic, since, divisions by a value close to zero will greatly increase high-frequency noise contribution.

To address this issue, among others, a Wiener filter could be used. Before going further, let us consider a discrete  $M \times N$  image  $f$ , defined on the image domain  $D_f$  and corrupted by additive white noise  $\eta$  with zero mean and variance  $\sigma_\eta^2$ . For each pixel  $(x,y)$ , we define the observed image  $f_n$  as  $f_n(x,y) = f(x,y) + \eta(x,y)$ . Using the linearity property in (7), the SSRT of the observed image  $f_n$  is given by

$$\mathcal{R}_\sigma[f_n](\rho, \theta) = \mathcal{R}_\sigma[f](\rho, \theta) + \mathcal{R}_\sigma[\eta](\rho, \theta) = (\mathcal{R}[f] *^\rho g)(\rho, \theta) + \mathcal{R}_\sigma[\eta](\rho, \theta) \quad (31)$$

and, for a given  $\theta$ , we can compact (31) to obtain

$$\mathcal{R}_{\theta,\sigma}^{f_n}(\rho) = (\mathcal{R}_\theta *^\rho g)(\rho) + \mathcal{R}_{\theta,\sigma}^\eta(\rho) \quad (32)$$

The formulae (32) represents a typical mathematical model for many imaging systems including Computed Tomography (CT), in which  $g$  is commonly known as the point spread function (PSF). This function being known, which consists, in our case, in Gaussian function, deconvolution operations permit to reverse the process in order to improve the resolution of the imaging system. In our case, the deconvolution consists in the estimation of the Radon projection from SSRT projection in presence of noise and Gaussian smoothing. Numerous algorithms could be developed to recover  $\mathcal{R}_\theta$  from (32). Examples include Wiener deconvolution [7, 8], Lucy-Richardson algorithm [9] and variational model [10, 11]. Wiener deconvolution applies a Wiener filter

inherent in the deconvolution to the observed noisy samples, enabling simultaneous reconstruction and denoising [8]. It is designed so that the expectation value of the Mean Square Error (MSE)  $\varepsilon = \mathbb{E}\{(\mathcal{R}_\theta(\rho) - \hat{\mathcal{R}}_\theta(\rho))^2\}$  is minimized where, the *hat* symbol is used to indicate the estimate of the noise-free Radon projection. By deriving the MSE minimization in the frequency domain, the 1-D Fourier transform, with regard to the variable  $\rho$ , of the unnoisy Radon projection estimate is given by [12]

$$\hat{P}_\theta(\omega) = H_W(\omega) P_{\theta,\sigma}^{f^n}(\omega) \quad (33)$$

where,  $P_{\theta,\sigma}^{f^n}(\omega)$  is the SSRT projection spectrum of the observed noisy image and  $H_W(\omega)$  is the frequency response of the Wiener filter, expressed as

$$H_W(\omega) = \frac{1}{G(\omega)} \frac{|G(\omega)|^2}{|G(\omega)|^2 + K} \quad (34)$$

where,  $K = \frac{P_w^\eta(\omega)}{P_w(\omega)}$  with  $P_w(\omega) = \mathbb{E}|P_\theta(\omega)|^2$  and  $P_w^\eta(\omega) = \mathbb{E}|P_{\theta,\sigma}^\eta(\omega)|^2$  are the mean power spectral densities of  $\mathcal{R}_\theta(\rho)$  and  $\mathcal{R}_{\theta,\sigma}^\eta(\rho)$ , respectively.

When there is zero noise, i.e.  $K = 0$ , the Wiener filter is simply the inverse filter. In practice, the quantities  $P_w^\eta(\omega)$  and  $P_w(\omega)$  are not know so  $K$  is set to a constant scalar which is determined empirically.

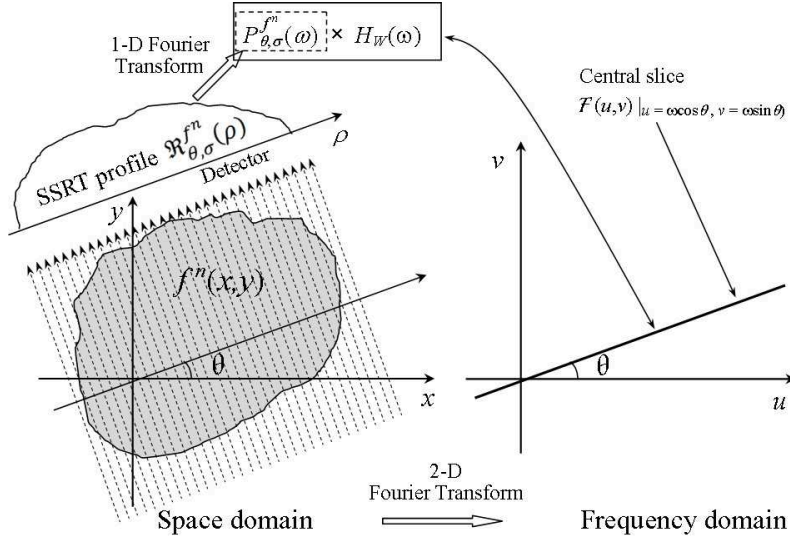


Figure 2: Illustration of Fourier Slice Transform in case of Scale Space Radon Transform

In case of SSRT, the FST synoptic scheme could be illustrated in Fig 2. So, by rotating the SSRT detector for  $180^\circ$ , the entire 2D Fourier transform  $\mathcal{F}(u, v)|_{u=\omega \cos \theta, v=\omega \sin \theta}$  is "measured". Once the 2D frequency space of the object function is filled, a 2-D inverse Fourier transform then yields the reconstructed object function, i.e.

$$f(x, y) = \int \int_{-\infty}^{+\infty} \mathcal{F}(u, v) e^{i2\pi(ux+vy)} du dv \quad (35)$$



The method of image reconstruction, depicted until now, is called on *Frequency-Domain Reconstruction*. As ascertained in [4], in practice, only a finite number of projections of an object can be taken. Then, the function  $\mathcal{F}(u, v)$  is only known along a finite number of radial lines such as in Fig. 3. To overcome this limitation and fill completely the 2D frequency space of the object function, very time-consuming operations of interpolation are required. Furthermore, since the density of the radial points becomes sparser as one gets farther away from the center, the interpolation error also becomes larger. These errors, implied in the high frequency domain, result in image degradation [4]. Consequently, the Frequency-Domain Reconstruction method is not used in practice.

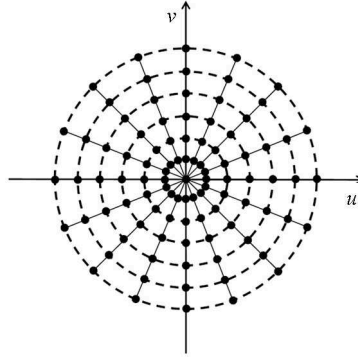


Figure 3: Sampling of the 2-D Fourier space of the object function.

#### 4.3. Filtered Backprojection (FBP) using SSRT for Parallel-Beam Geometry

As with Radon transform, the FST will be applied on the SSRT projections to derive the FBP algorithm. This derivation is based on the reformulation of the Fourier Slice theorem into polar coordinates, yielding a 2-step reconstruction method: a projection filtering and a backprojection onto the image domain.

The 2D inverse Fourier transform of  $\mathcal{F}(u, v)$  is

$$f(x, y) = \mathcal{F}^{-1}\{\mathcal{F}(u, v)\} = \int \int_{-\infty}^{+\infty} \mathcal{F}(u, v) e^{i2\pi(ux+vy)} du dv \quad (36)$$

Expressing this equation in a polar coordinate system  $(\omega, \theta)$  with  $u = \omega \cos \theta, v = \omega \sin \theta$  and  $du dv = \omega d\omega d\theta$ , yields

$$f(x, y) = \int_0^{2\pi} \int_0^{+\infty} \mathcal{F}_{polar}(\omega, \theta) e^{i2\pi\omega(x\cos\theta+y\sin\theta)} \omega d\omega d\theta \quad (37)$$

Splitting the outer integral domain into  $[0, \pi)$  and  $[\pi, 2\pi)$ , and using  $\mathcal{F}_{polar}(\omega, \theta + \pi) = \mathcal{F}_{polar}(-\omega, \theta)$  yields

$$f(x, y) = \int_0^{\pi} \left[ \int_{-\infty}^{+\infty} \mathcal{F}_{polar}(\omega, \theta) |\omega| e^{i2\pi\omega(x\cos\theta+y\sin\theta)} d\omega \right] d\theta \quad (38)$$

According to the FST proposal (28) and the RT/SSRT relationship in frequency domain provided in (33), we obtain

$$f(x, y) = \int_0^\pi \left[ \int_{-\infty}^{+\infty} P_{\theta, \sigma}^{f_n}(\omega) H_W(\omega) |\omega| e^{i2\pi\omega(x\cos\theta + y\sin\theta)} d\omega \right] d\theta \quad (39)$$

The integral in (39) may be expressed as

$$f(x, y) = \int_0^\pi Q_{\theta, \sigma}(x\cos\theta + y\sin\theta) d\theta \quad (40)$$

where

$$Q_{\theta, \sigma}(\rho) = \int_{-\infty}^{+\infty} P_{\theta, \sigma}^{f_n}(\omega) H_W(\omega) |\omega| e^{i2\pi\omega\rho} d\omega \quad (41)$$

The formulae (41) represents a filtering operation, where the frequency response of the filter is given by  $H_s(\omega) = |\omega|H_W(\omega)$  whilst, (40) represents the backprojection of the filtered projections. The resulting projections for the different angles  $\theta$  are stacked to form the estimate of  $f(x, y)$  which represents the reconstructed image. Let recall, as seen in literature, that the *ramp* filter, with frequency response  $H(\omega) = |\omega|$ , is retrieved in the FBP reconstruction algorithm, used for RT inversion. However, according to the present founding, it is important to note that, in case of SSRT, the FBP procedure leads to a convolution of the projections with a filter kernel  $h_s$  of which the frequency response is equal to the product  $H_s(\omega) = H(\omega)H_W(\omega)$ . According to the reasoning developed until now, we have considered the idealized case where there is a continuum of projection views. In practice, since the image function is discrete and bounded, the sinograms have only a finite number of angular and radial samples. Then, the formula (41) and (40) dealing with the FBP reconstruction method using SSRT require modification for practical implementations. In this work, the discrete approximations used in [4, 13] are the basis of the reconstruction algorithm, depicted above.

As  $H_s(\omega)$  is not absolutely integrable, it is not possible to derive directly the corresponding impulse response by the inverse Fourier transform. To address this issue, we have to window the filter so that it becomes zero outside a defined frequency interval.

Suppose that  $\mathcal{R}_\theta(\rho)$  is band-limited with maximum frequency less than  $\omega_{max} = \frac{1}{2\tau}$  where,  $\tau$  is the sampling interval with which the projection data are measured. Then,

$$H_s(\omega) = \begin{cases} |\omega|H_W(\omega), & |\omega| < \omega_{max} \\ 0, & \text{otherwise.} \end{cases} \quad (42)$$

An example of frequency response for  $H_s(\omega)$  is given in Fig. 4 where, the constant  $K$  and the Gaussian kernel standard deviation  $\sigma$ , for the Wiener filter, are set to 0.02 and 1.5, respectively.

It is known that the ramp filter  $H(\omega) = |\omega|$  amplifies high frequency noise, so the low-pass Wiener filter  $H_W$  is used, here, as a smoothing filter.

The steps of the FBP method dealing with the SSRT projections are summarized as follows.

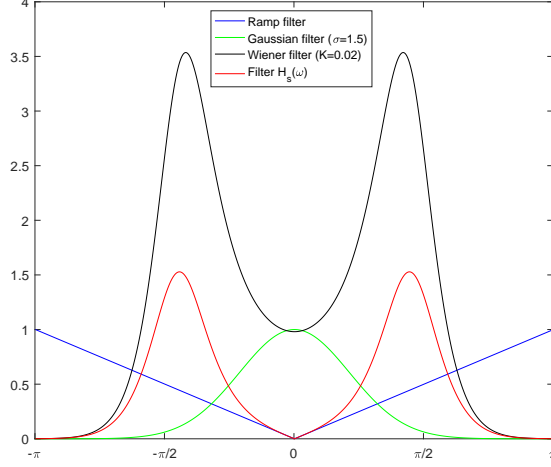


Figure 4: Example of the filter response  $H_s(\omega)$  (in red line) for the FBP reconstruction using SSRT with  $\sigma = 1.5$  and  $K = 0.02$

- **Step 1:** Compute the 1-D Fourier transform  $P_{\theta,\sigma}^{f_n}(\omega)$  of each SSRT projection for the observed image.
- **Step 2:** Multiply each SSRT projection spectrum by the Wiener filter  $H_W(\omega)$  to obtain the spectrum estimate  $\hat{P}_\theta(\omega)$  of the unnoisy Radon projection, as in (33).
- **Step 3:** Multiply  $\hat{P}_\theta(\omega)$ , for each  $\theta$ , by the 1-D windowed ramp filter function  $H(\omega) = |\omega|$
- **Step 4:** Perform a 1-D inverse Fourier transform of the resulting filtered data using (41).
- **Step 5:** Perform the backprojection by integrating, over  $\theta$ , all the 1-D inverse transforms from Step 4 using (40).

## 5. Experiments

The proposed Filtered Backprojection method using SSRT projections, of which the steps are summarized in Sect. IV.C, is denoted SSRT-FBP. In order to show the effectiveness of this method in the tomographic image reconstruction, let us compare its performance to: (1) the SSRT inversion scheme given at Sect. IV.A, denoted Deconv-Rad-FBP and (2) the classical FBP-based inverse Radon transform, denoted Radon-FBP. Because of its widespread utilization in the evoked domain, a Shepp-Logan phantom of size  $M \times N = 512 \times 512$  is used for experimental analysis. It is transformed by SSRT and RT to provide sinograms on  $180^\circ$  with angular step  $\Delta\theta = 0.5^\circ$ , used as input projections. As seen in the previous sections, the SSRT projections magnitude depend

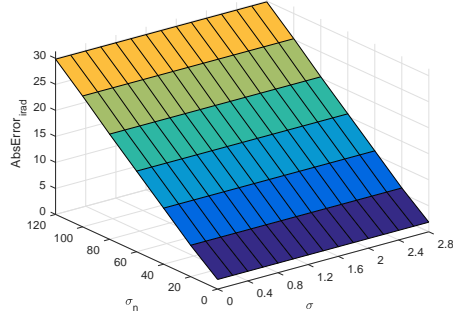
on the standard deviation  $\sigma$  of the Gaussian function involved in SSRT. That is why, to see its influence on the outcomes, a range of values, varying from  $\sigma \sim 0$  to  $\sigma = 2.8$  with a step of  $\Delta\sigma = 0.2$ , is considered in these experiments. The influence of additive noise on the input images is also examined. An image  $f_n$  damaged by additive white Gaussian noise (AWGN) with standard deviation  $\sigma_n$  can be modeled by  $f_n = f + \sigma_n \varepsilon$  where,  $f$  is the noise-free image and  $\varepsilon$  is the realization of a normalized zero-mean Gaussian random vector. In these experiments, we take  $\sigma_n \in \{20, 40, 60, 80, 100, 120\}$ . The reconstructed images by the methods Radon-FBP, Deconv-Rad-FBP and SSRT-FBP are denoted by the 2D functions  $f^{iRad}$ ,  $f^{deconv+iRad}$  and  $f^{iSSRT}$ , respectively. Well-known metric of Mean Absolute Error (MAE) is used to evaluate the quality of the above-mentioned image reconstruction methods. Here,  $MAE_k = \sum_i \sum_j |f_{ij} - f_{ij}^k| / MN$  where,  $f$  is the free-noise Shepp-Logan phantom and  $k \in \{iRad, deconv + iRad, iSSRT\}$ . To assure the statistical validity of the experiments since the noise is generated randomly, the experiments are carried out  $N_r$  times ( $N_r = 20$ ) and the average result is taken. For the Wiener filter, a value of  $K$  equal to 0.02 reveals to be sufficient to make a trade-off between the image sharpening effects and the smoothing ones. For all methods, the running time is expressed in *seconds* (s) and the implementations are performed in Matlab environment on a HP/Z2 Workstation with Intel Xeon 3.40 GHz CPU and 32 GB RAM. Figs. 5 depict the MAE values by browsing  $\sigma$  and  $\sigma_n$  on their value interval. It is worth to note that, although the Radon-FBP method is not concerned by  $\sigma$ , the latter is just included in the MAE graphics for comparison reasons. We remark, here, that for both SSRT-based methods (Deconv-Rad-FBP, SSRT-FBP), the image reconstruction scores are better than those of FBP-Radon method. Concerning comparison between SSRT-FBP and Deconv-Rad-FBP, it is noted that the former is better for SSRT with fairly large Gaussian ( $\sigma \gtrsim 0.7$ ), in presence of additive noise ( $\sigma_n \gtrsim 15$ ), as depicted in Fig. 5.e.

The reconstructed images with methods of Radon-FBP, Deconv-Rad-FBP and SSRT-FBP are illustrated in Fig. 6.b-d, respectively, for  $\sigma = 1.2$  and  $\sigma_n = 30$ . In Fig. 6.e, the Shepp-Logan image gray level profiles, for unnoisy image, noisy image and reconstructed images, are highlighted. We remark, at first, that the effect of noise is attenuated for all the used methods, which is expected since RT and SSRT are robust to additive noise [14, 1]. By examining the profiles, it appears that the smoothing effect is more pronounced for SSRT-FBP method w.r.t. Deconv-Rad-FBP and Radon-FBP methods where, for the latter, the smoothing is the lowest.

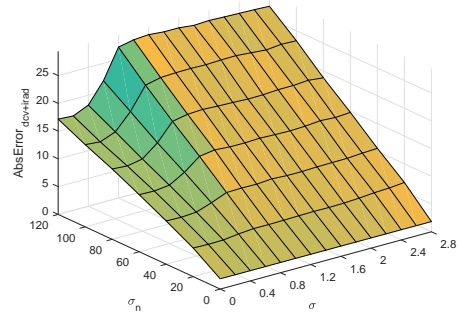
In terms of execution speed, the SSRT-FBP method is comparable with Radon-FBP with runtime around 0.1 s, as read in Table 1. However, the algorithm applied in Deconv-Rad-FBP method requires much more time which approximates 4.7 s.

Table 1: Image reconstruction runtime scores

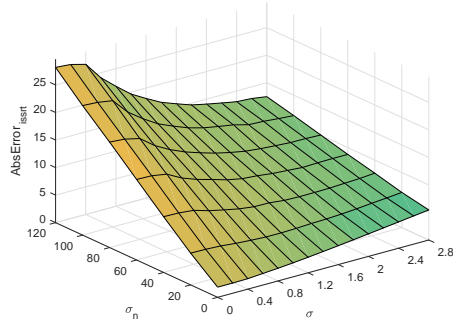
|             | Radon-FBP | Deconv-Rad-FBP | SSRT-FBP |
|-------------|-----------|----------------|----------|
| Runtime (s) | 0.107     | 4.737          | 0.102    |



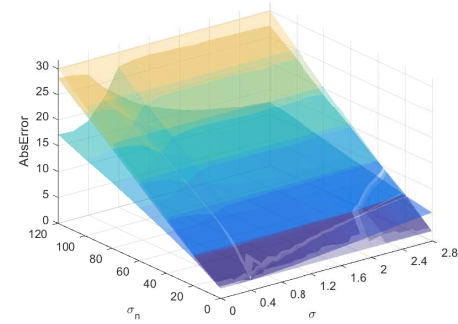
(a) Radon-FBP



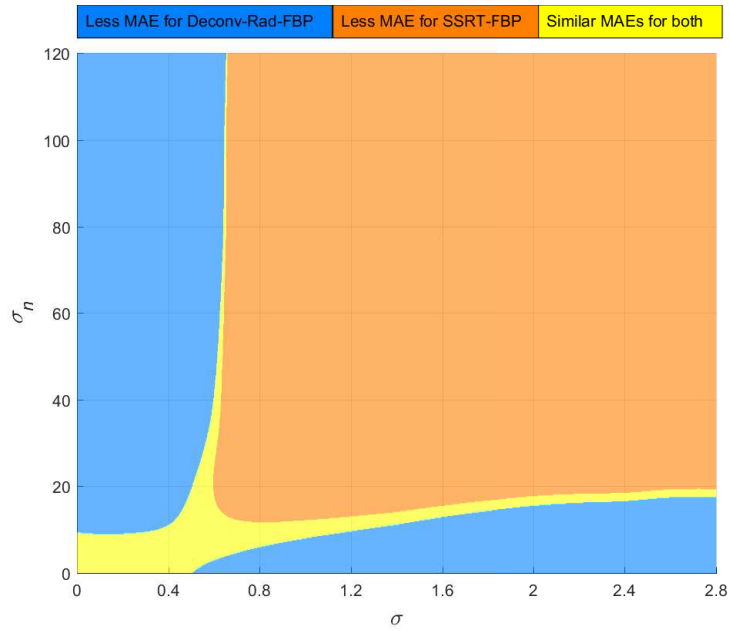
(b) Deconv-Rad-FBP



(c) SSRT-FBP



(d) All MAEs stacked together



(e) Case of Deconv-Rad-FBP vs SSRT-FBP

Figure 5: Mean absolute errors for the reconstructed Shepp-Logan head phantom image in function of  $\sigma_n$  and  $\sigma$

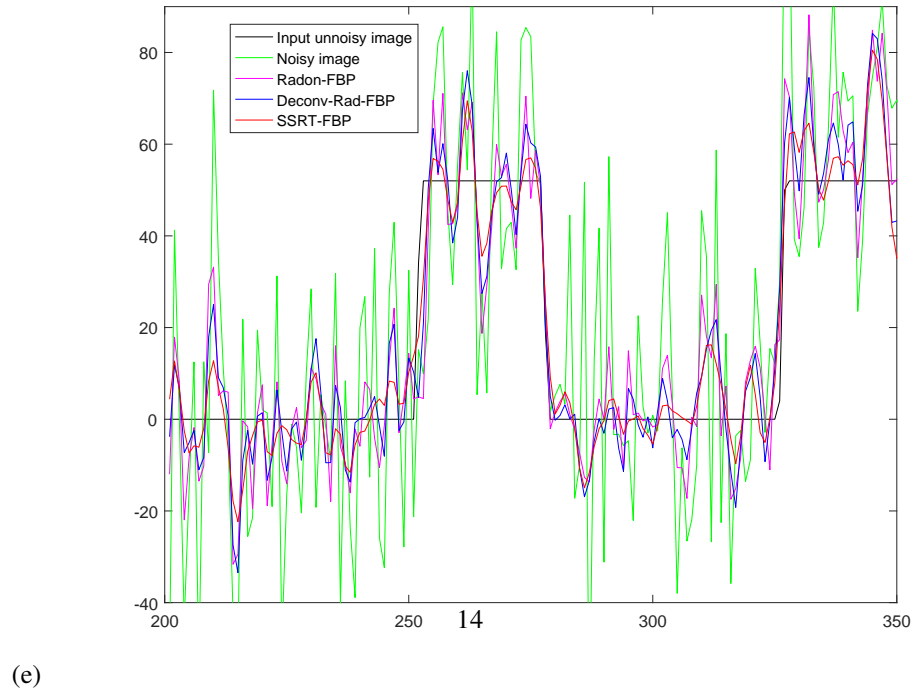
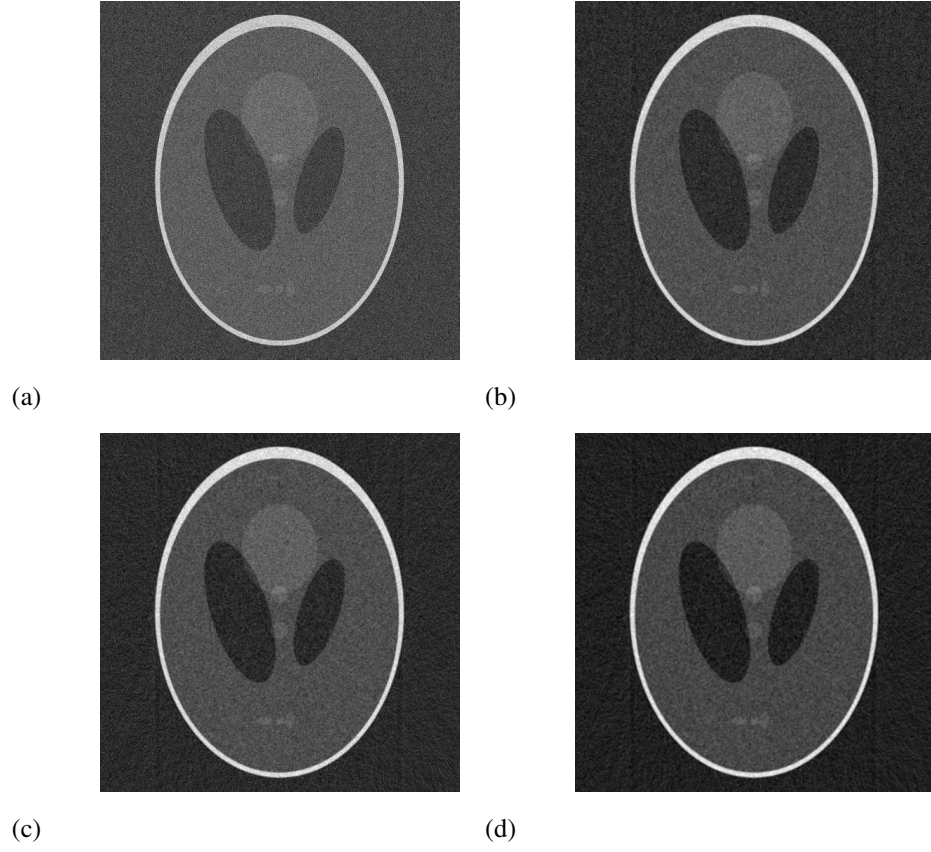


Figure 6: Image reconstruction results with  $(\sigma, \sigma_n) = (1.2, 30)$ . (a) Input Shepp-Logan phantom image corrupted by AGWN with  $\sigma_n = 30$ , (b) Radon-FBP, (c) Deconv-Rad-FBP, (d) SSRT-FBP and (e) A part of noise-free, noisy and reconstructed noisy image profiles (row #300 vs columns #200...#350)

## 6. Conclusion

In this paper, we have, first, presented the basic properties and the inversion approaches of the Scale Space Radon Transform. Afterwards, we have, originally, adapted the Filtered Backprojection to be applied on SSRT for the reconstruction of the Shepp-Logan head phantom image, corrupted by additive white noise. The results are compared with the FBP applied on Radon transform and another scheme of SSRT inversion consisting in an image deconvolution to recover Radon sinogram followed by classical FBP. Using the Mean Absolute Error as quality measure, the preliminary results show the high performance of SSRT-based image reconstruction techniques with regards to the RT-based one. Especially, the FBP technique using SSRT yields small computation time and less errors for high levels of noise when the Gaussian kernel standard deviation is higher than 0.7.

## References

### References

- [1] D. Ziou, N. Nacereddine, A. B. Goumeidane, Scale space radon transform, *IET Image Processing* 15 (9) (2021) 2097–2111. doi:10.1049/ipr2.12180.
- [2] S. R. Deans, *The Radon transform and some of its Applications*, John Wiley & Sons Ed., NY, USA, 1983.
- [3] D. E. Dudgeon, R. M. Mersereau, *Multidimensional digital signal processing*, Prentice-Hall, Englewood Cliffs, NJ, USA, 1984.
- [4] M. Kak, A. C. and Slaney, *Principles of Computerized Tomographic Imaging*, IEEE Press, NY, USA, 1988.
- [5] F. Orieux, J.-F. Giovannelli, T. Rodet, Bayesian estimation of regularization and point spread function parameters for wiener–hunt deconvolution, *J. Opt. Soc. Am. A* 27 (7) (2010) 1593–1607. doi:10.1364/JOSAA.27.001593.
- [6] J. Jan, *Medical Image Processing, Reconstruction and Restoration: Concepts and Methods*, Taylor & Francis Ltd, Boca Raton, FL, USA, 2006.
- [7] N. Wiener, *Extrapolation, Interpolation and Smoothing of Stationary Time Series with Engineering Applications*, MIT Press, Cambridge, MA, USA, 1949.
- [8] A. P. Dhawan, R. M. Rangayyan, R. Gordon, Image restoration by wiener deconvolution in limited-view computed tomography, *Appl. Opt.* 24 (23) (1985) 4013–4020. doi:10.1364/AO.24.004013.
- [9] W. H. Richardson, Bayesian-based iterative method of image restoration, *J. Opt. Soc. Am.* 62 (1) (1972) 55–59. doi:10.1364/JOSA.62.000055.
- [10] Y.-L. You, M. Kaveh, Anisotropic blind image restoration, in: *Proceedings of 3rd IEEE International Conference on Image Processing*, Vol. 2, 1996, pp. 461–464. doi:10.1109/ICIP.1996.560885.

- [11] M. Welk, A robust variational model for positive image deconvolution, *Signal, Image and Video Processing* 10 (2) (2016) 369–378. doi:10.1007/s11760-015-0750-z.
- [12] R. Gonzalez, R. Woods, *Digital Image Processing*, 2nd Edition, Prentice Hall, Englewood Cliffs, NJ, USA, 2002.
- [13] J. Fessler, Analytical tomographic image reconstruction methods, Tech. rep., University of Michigan, Ann Arbor, MI (2009).  
URL <https://web.eecs.umich2016edu/~fessler/course/516/1/c-tomo.pdf>
- [14] N. Nacereddine, S. Tabbone, D. Ziou, Robustness of radon transform to white additive noise: general case study, *Electronics Letters* 50 (15) (2014) 1063–1065. doi:10.1049/el.2014.0626.